Orbital, Rotational and Climatic Interactions: Energy Dissipation and Angular Momentum Exchange in the Earth-Moon System

Final Report

Principal Investigator: Gary D. Egbert

09/15/97—09/14/01

College of Oceanic and Atmospheric Sciences
Ocean Administration Building 104
Oregon State University
Corvallis, OR¡ 97331-5503

Grant Number: NAG5-6156

1 Summary

A numerical ocean tide model has been developed and tested using highly accurate TOPEX/Poseidon (T/P) tidal solutions. The hydrodynamic model is based on time stepping a finite difference approximation to the non-linear shallow water equations. Two novel features of our implementation are a rigorous treatment of self attraction and loading (SAL), and a physically based parameterization for internal tide (IT) radiation drag. The model was run for a range of grid resolutions, and with variations in model parameters and bathymetry. For a rational treatment of SAL and IT drag, the model run at high resolution (1/12 degree) fits the T/P solutions to within 5 cm RMS in the open ocean. Both the rigorous SAL treatment and the IT drag parameterization are required to obtain solutions of this quality. The sensitivity of the solution to perturbations in bathymetry suggest that the fit to T/P is probably now limited by errors in this critical input. Since the model is not constrained by any data, we can test the effect of dropping sea-level to match estimated bathymetry from the last glacial maximum (LGM). Our results suggest that the $\approx$ 100 m drop in sea-level in the LGM would have significantly increased tidal amplitudes in the North Atlantic, and increased overall tidal dissipation by about 40%. However, details in tidal solutions for the past 20 ka are sensitive to the assumed stratification. IT drag accounts for a significant fraction of dissipation, especially in the LGM when large areas of present day shallow sea were exposed, and this parameter is poorly constrained at present.

2 Introduction

The evolution of the mooon's orbit around the Earth is closely linked to the history of tidal dissipation in the ocean (e.g., Bills, and Ray, 1999). This connection, and the clear evidence that tidal dissipation must have varied significantly over time, have spurred a number of efforts to model the ocean tides in the recent and distant past (e.g., Thomas and Sundermann; 1999; and references therein). It is far from clear how reliable these modeling studies are, given that bathymetry in the past is only known approximately, and given the challenges in numerical modeling of even the modern day tides.

With the availability of TOPEX/Poseidon (T/P) altimeter data, barotropic tidal elevations in the open ocean are now known to within roughly 1 cm (Shum et al., 2000). However, to obtain solutions with this accuracy it has been necessary to use some sort of data assimilation or empirical mapping approach (e.g., Egbert et al., 1994; Schrama and Ray, 1994). The results of Le Provost et al. (1994) with the finite element hydrodynamic model FES94 suggested that accuracies approaching the empirically constrained solutions could be obtained with a purely hydrodynamic model, if high enough numerical resolution were used. However, in this work modeling was accomplished separately for individual

ocean basins, and the results were spliced together. Open boundary conditions for each basin were adjusted to achieve agreement with tide gauges, sometimes even using a strong constraint data assimilation approach (Lyard and Genco, 1994), so these solutions were not really independent of observational data. Subsequent improvements to the Grenoble modeling code have allowed simultaneous modeling of the full globe with no adjustable open boundary conditions. The resulting global solutions fit validation tide gauges much more poorly (F. Lyard, personal communication), demonstrating the critical role played by data in FES94.

There is now strong evidence that significant energy is transfered from barotropic to internal tides over rough topography in the deep ocean (Egbert and Ray, 2000; 2001). Since this "internal tide drag" appears to account for about 1/3 of the total tidal dissipation, accurate modeling of the barotropic tide almost certainly will require accounting for this conversion, either by modeling the full three-dimensional stratified ocean, or by some sort of parameterization (Jayne and St. Laurent, 2001). Only the later approach is computationally feasible at this time.

In this report we describe our efforts to develop a global barotropic hydrodynamic model which reproduces the present day tidal elevation fields using only the astronomical forcing, with no data assimilation or boundary condition constraints. We use a straightforward modeling approach, based on finite difference time-stepping of the non-linear barotropic shallow water equations (SWE), with a rigorous treatment of ocean self attraction and loading (SAL) effects, and several parameterizations of internal tide (IT) drag. Computations are done for a wide range of nearly global model grids, with resolutions ranging from 1°–$1/12^{\circ}$. We also do experiments with small perturbations to our standard bathymetry, to test sensitivity of solutions to this critical input parameter. For all of the results reported here we focus on the principal lunar constituent M_2, but other constituents were included in the modeling effort. As we shall show, including a parameterization for IT drag significantly improves the fidelity of the solution. The best model results (5 cm RMS misfit between deep-ocean T/P elevations and the numerical model) are obtained with the highest resolution grid, and with rigorous treatment of ocean self-attraction and loading. The level of accuracy achieved is in fact reasonably consistent with the effect of likely errors in the currently best available bathymetry.

Finally, we consider the effect of dropping sea-level to that estimated for the last glacial maximum (LGM). The IT drag parameterization we use depends on ocean stratification, and it is not clear how this effect should be modeled for the LGM. We test several scenarios, including stratification similar to the modern ocean, and significant reductions and increases in stratification. As we shall show, the effects of LGM sea-level changes are much larger than errors in the modern solutions. In particular, tidal dissipation increases by up to 50% in the LGM. However, the sensitivity of the model results to both bathymetry and stratification suggests that efforts to accurately model tidal dissipation in even the recent past remain very challenging.

3 Hydrodynamic Modeling

3.1 Finite-difference SWE

We assume shallow water dynamics of the form

$$\frac{\partial \mathbf{U}}{\partial t} + \mathbf{f} \times \mathbf{U} + \mathbf{U} \cdot \nabla \mathbf{U} + a_H \nabla^2 \mathbf{U} + gH\nabla(\zeta - \zeta_{\mathrm{SAL}}) + \mathcal{F} = \mathbf{f}_0 \tag{1}$$

$$\frac{\partial \zeta}{\partial t} = -\nabla \cdot \mathbf{U}. \tag{2}$$

Here ζ is the tidal elevation; $\mathbf{U}$ is the volume transport vector, equal to velocity times water depth H; $\mathbf{f}$ is the Coriolis parameter (oriented to the local vertical), $\mathcal{F}$ is the frictional or dissipative stress, and the term $a_H \nabla^2 \mathbf{U}$ is a crude parameterization of horizontal turbulent eddy viscosity, included primarily to improve numerical stability. For most of the results discussed here we have taken $a_H = 10^3 m^2 s^{-1}$. Elevations in the open ocean were found to be insensitive to the exact value of this parameter unless it was significantly increased (e.g., to $10^5 m^2 s^{-1}$). The global solution is also only weakly dependent on inclusion of the non-linear terms in (1). The astronomical tide generating force, which includes the Earth's body tide (Hendershott, 1972) is denoted by $\mathbf{f}_0$. We included up to 8 constituents (M_2, S_2, N_2, K_2, K_1, O_1, P_1 Q_1) in $\mathbf{f}_0$. However, very similar results were obtained (for M_2) when the forcing was restricted to the dominant semi-diurnal and diurnal constituents M_2 and K_1, so only these two constituents were used for most of the extensive modeling experiments described here.

Tidal loading and self-attraction (Hendershott, 1972; Ray, 1998) are accounted for by the term ζ_{SAL}, which we discuss in detail below. We solve the system of equations (1) and (2) numerically on a C-grid, following the finite difference time-stepping approach described in Egbert et al. (1994).

All grids were nearly global, covering the area from 86°S to 82.25°N. Bathymetry was interpolated (and smoothed where appropriate) from a combination of the 1/30 degree database of Smith and Sandwell (1997) in deep water equatorward of 72°, ETOPO5 (National Geophysical Data Center, 1992) in shallow areas and the Arctic, and a new compilation of bathymetry for the Antarctic (L. Padman, personal communication). Open boundary conditions at the top of the domain in the Arctic were specified elevations, taken from the global FES94 solution (Le Provost et al., 1994), Tests with variants (including the Arctic assimilation solutions of Kivman (1997)) showed that elevations outside the arctic were nearly independent of the details in these boundary conditions. Boundary conditions at the coast were zero normal flow, and no slip.

The dissipation term $\mathcal{F} = \mathcal{F}_B + \mathcal{F}_{IT}$ included components for bottom boundary layer drag and IT wave radiation. The first (and standard) component was parameterized in

the usual way as quadratic in velocity

$$\mathcal{F}_B = (c_D||\mathbf{v}||/H)\mathbf{U}, \tag{3}$$

where $\mathbf{v}$ is the total velocity vector (in particular, including all tidal constituents), and the value of the non-dimensional parameter c_D is approximately 0.0025. Test with a range of values for c_D showed that deep-water elevations were only weakly sensitive to the value of this parameter. Several different parameterizations of IT wave drag were tried.

3.2 Parameterization of Internal Tide Drag

Jayne and St. Laurent (2001) describe a simple parameterization of IT drag based on a linear analysis of energy flux into the internal wave field due originally to Bell (1975). In this theory energy conversion from barotropic to baroclinic tides by small amplitude sinusoidal topography of amplitude h and wavenumber κ is

$$E_f = \frac{(\omega^2 - f^2)^{1/2}}{2}\rho_0 \kappa h^2 N u^2, \tag{4}$$

where N is the buoyancy frequency, ρ_0 the mean ocean density, f the Coriolis parameter, ω the tidal frequency, and u the barotropic tidal velocity perpendicular to the topography. Since the theory is linear, superposition may be used to estimate conversion for more complex topographic variations. To apply (4) Jayne and St. Laurent (2001) estimated the height of the scattering topography as the RMS of bathymetric variations not resolved by their $1/2^\circ$ numerical grid, and, ignoring the dependence on tidal frequency ω, obtained a spatially varying linear drag coefficient

$$c_{IT} = \frac{1}{2H}\kappa h^2 N. \tag{5}$$

The buoyancy frequency N (for the ocean bottom) was obtained from Levitus (1999), the wavenumber κ was left as a tunable parameter, and the linear dissipation term $\mathcal{F}_{IT} = c_{IT}\mathbf{U}$ was then added to the quadratic bottom drag (3). Note that c_{IT} is just the linear drag coefficient required to match the energy loss to the barotropic tide predicted by the simple theory of Bell (1975). Jayne and St. Laurent (2001) found that including this extra term in their implementation of the linear SWE (with $\kappa \approx 2\pi/10$km) significantly improved fit of modeled tidal elevations to those estimated from T/P.

We implemented and tested the scheme of Jayne and St. Laurent (2001), along with two variants. The first of these is based on the work of Sjoberg and Stigebrandt [1992], who give an alternative (but dimensionally similar) expression for barotropic energy conversion. In this approach the conversion (comparable to E_f of (4)) is calculated by treating the bottom topography as a series of discrete steps, and applying theories developed for generation of internal waves by flow over sills. Note that in this approach energy

conversion is calculated for each step independently, and that this can only be formally justified if the steps are far enough apart. Expressions for energy flux away from each topographic step are given in Sjoberg and Stigebrandt (1992) and are summarized in Gustafson (2001). The resulting expressions for E_f again depend quadratically on the cross-step tidal velocity, so a linear drag coefficient c_{IT} is readily derived as for the Bell formula (4). This second approach has no obvious unknown or tunable parameters, but in fact the expression for E_f can be shown to depend strongly on the grid resolution used to define the steps (Garrett et al., 2002). For our calculations we used a $1/12^{\circ}$ grid to define the topographic steps, and stratification profiles from Levitus (1999) to compute the IT drag. In numerical experiments with this parameterization it was found necessary to allow for an extra tunable scaling factor to obtain the best results.

The final approach we tried is based on an extension of the theory of Bell to allow for two–dimensional topography and a finite–depth ocean (Llewellyn Smith and Young; 2001). As with Bell (1975) the theory is linear and inviscid, and small amplitude topography is assumed on an otherwise flat bottom. A rigid lid is assumed at the sea-surface. The internal tide is forced by the barotropic component of vertical velocity (e.g., Baines, 1982) $w_{BT}(z) = \mathbf{u} \cdot \nabla H z/H$ where $-H \leq z \leq 0$, and $\mathbf{u}$ is the depth independent barotropic horizontal velocity. As shown in Llewellyn Smith and Young (2001) the baroclinic bottom pressure $p_{BC}(-H)$ can be given as the convolution of a radially symmetric Green's function $\mathcal{G}_\omega(s)$ and the barotropic vertical velocity at the bottom $p_{BC}(-H) = \mathcal{G}_\omega * w_{BT}(-H)$. Note that in our notation the Green's function gives the internal wave bottom pressure as a function of distance from a "unit magnitude" point source forcing velocity profile (at frequency ω) of the form $w_{BT}(z) = -z/H$. The Green's function can be written down analytically in terms of the flat bottom vertical mode eigenvalues and eigenvectors. A slightly simplified version, based on a WKB approximation to the vertical modes can be given explicitly as

$$\mathcal{G}_\omega(s) = \frac{(\omega^2 - f^2)N_B}{g} \sum_n H_2^0 \left(n\pi(\omega^2 - f^2)^{-1/2} s/H\bar{N} \right), \tag{6}$$

where H_2^0 is the zero order Hankel function of the second kind, and s denotes radial distance (Llewellyn Smith and Young, 2001). The barotropic/baroclinic energy at a fixed location is then readily calculated as

$$E_f = \langle p_{BC}(-H) w_{BT}(-H) \rangle, \tag{7}$$

where the brackets denote tidal cycle averages. Further details, and exact expressions (without the WKB approximation) are given in Llewellyn Smith and Young (2001).

This theory allows an explicit formulation for the dependence of IT drag on the barotropic velocity which is rigorously justifiable for the case of small amplitude bottom topography (and laterally homogeneous stratification)

$$E_f = \left\langle \mathbf{u} \cdot (\nabla H)^T \mathcal{G}_\omega(s) * \nabla H \mathbf{u} \right\rangle = \langle \mathbf{u} \cdot \mathcal{R}_\omega * \mathbf{u} \rangle . \tag{8}$$

From (8) we see that for a fixed frequency ω the IT drag component of the dissipative stress $\mathcal{F}$ in (1) can be represented as $\mathcal{F}_{IT} = H^{-1}\mathcal{R}_\omega * \mathbf{U}$. This is linear in the transports $\mathbf{U} = H\mathbf{u}$, but is non-local in space. Note also that this dissipation operator is frequency dependent, and hence also non-local in time. As it would be extremely expensive to fully implement this in a numerical scheme for solving the time dependent SWE, we implemented this scheme only approximately. First, as we focus primarily on the M_2 tide, we take $\omega = 1.4052 \times 10^{-4}\mathrm{s}^{-1}$ as a constant. Second, we do the convolution in space once, using the frequency domain barotropic tidal velocity fields $\mathbf{u}$ from a numerical model to calculate $E_f(\theta, \phi)$ as a function of position using (7). Then, we replace convolution with $\mathcal{R}_\omega$ by multiplication with the 2×2 spatially varying drag tensor

$$\mathbf{R}(\theta, \phi) = E_f(\theta, \phi) \, |\mathbf{u} \cdot \nabla H|^{-2} \, (\nabla H)^T \nabla H. \tag{9}$$

Note that $\mathbf{R}$ is singular, since conversion to baroclinic motions occurs only for motions perpendicular to local bathymetric gradients.

The approximate linear 2×2 drag tensor $\mathbf{R}$ will result in the correct energy dissipation at each point provided the tidal velocities in the numerical solution are exactly equal to the *a priori* assumed $\mathbf{u}$ in (9). For our calculation we computed $\mathbf{u}$ by solving the SWE in a series of small overlapping rectangular areas, each 20° on a side, with grid resolution of $1/30^\circ$, and open boundary conditions from the global inverse solution TPXO.5 (Egbert and Erofeeva, 2002). These local solutions are in fact quite similar to TPXO.5. The resulting approximate drag tensors $\mathbf{R}$ are thus most appropriate for open ocean tidal velocities of the modern ocean. Some thoughts on possible refinements of this procedure will be given below. The amplitude of the drag tensor (i.e, the sum of the diagonal elements of $H^{-1}\mathbf{R}$) is plotted on a logarithmic scale in Figure 1. The computed IT drag is largest in the open ocean over rough topography, in most of the same areas where Egbert and Ray (2000, 2001) found significant dissipation in the barotropic tide. The IT drag coefficient is also often large along the continental shelf break, but note that in these areas tidal volume transports, and hence E_f, are typically not so large.

Note that the spatial pattern of IT drag coefficients are very similar for all three approaches tried. This is not surprising since in all cases the estimated energy fluxes scale quadratically with topographic slope and tidal velocity, and linearly with bottom stratification, as in (4).

3.3 Implementation of the SAL Correction

In (1) the effects of ocean self–attraction and loading (SAL) are included as an extra equilibrium–like tide ζ_{SAL}. This can be related to the tidal elevation ζ through convolution (on the sphere) with the SAL Green's function (e.g., Hendershott, 1972; Ray, 1998)

$$\zeta_{\mathrm{SAL}} = \mathcal{G}_{SAL} * \zeta. \tag{10}$$

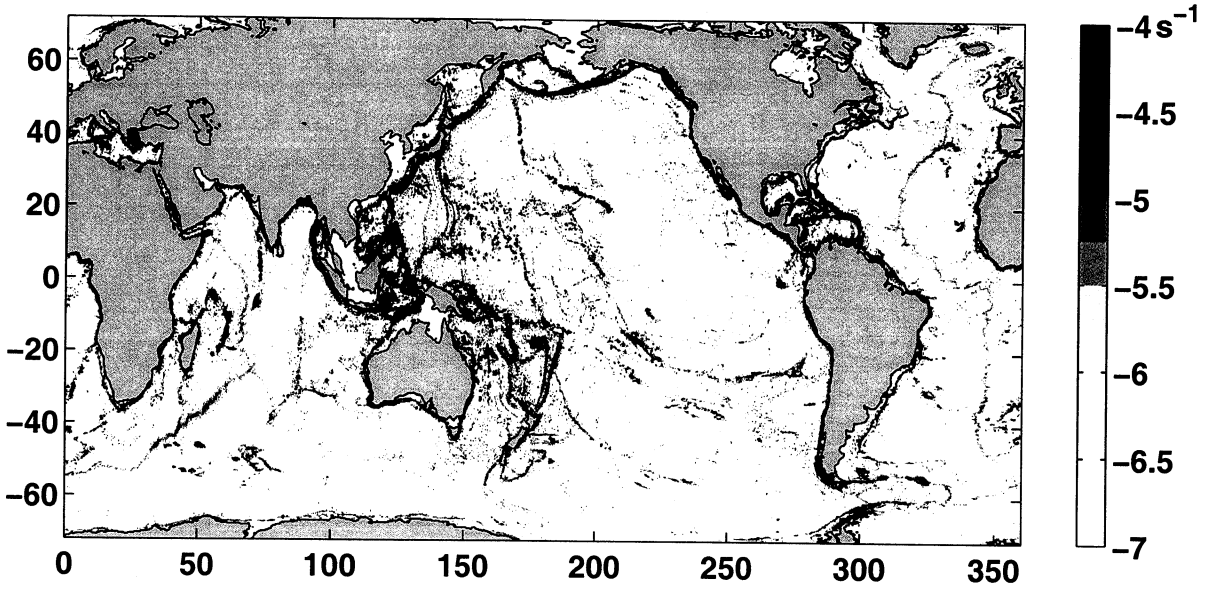

Figure 1: Amplitude of the internal tide drag tensor $H^{-1}\mathbf{R}$ for M_2.

Substituting (10) into (1) results in an integro–differential equation. A naive solution approach, applying the full convolution operator of (10) at each time step, would obviously not be computationally practical. For the modern day ocean ζ is well known (at least in the open ocean) so ζ_{SAL} can be computed once and added to (1) as an extra forcing term This approach, with elevations from Schwiderski (1978), was used by Le Provost et al. (1994). However, solutions computed in this way are not really independent of all data, and the computed elevation fields will not in general be consistent with the assumed ζ_{SAL}. This inconsistency can lead to significant imbalances in the energy equation (e.g., Le Provost and Lyard, 1997). This simple approach is of course even harder to justify for calculations with different ocean geometries, where tidal elevations may be expected to deviate from the modern estimates of ζ used to compute ζ_{SAL}.

Another simple approach that has frequently been used is to approximate convolution with $\mathcal{G}_{SAL}$ with multiplication by a scalar factor β. In this case $\zeta - \zeta_{\text{SAL}}$ is replaced by $(1-\beta)\zeta$ and (1) is reduced to a partial differential equation. Analysis by Accad and Pekeris (1978) suggested $\beta \approx 0.085$; Schwiderski (1978) used $\beta = 0.1$. However, as pointed out by Ray (1998) no fixed scalar β is appropriate for all locations in the ocean. Our own experiments suggested that this scalar approach could result in significant errors in global tidal solutions. To allow rigorous treatment of SAL in global modeling Hendershott (1972) suggested an iterative approach, with elevations ζ^n from iteration n being used in (10) to compute ζ^n_{SAL}, and then the result used in (1) to compute a new solution ζ^{n+1}. However, numerical experiments with this approach suggested that convergence of this iterative scheme could not be guaranteed (Hendershott, 1972; 1977). We tried this iterative scheme for modern ocean basins, starting from an initial guess at ζ^0_{SAL} estimated

from an accurate T/P based model (TPXO.5). In Figure 2a we plot (dashed line) the RMS change in elevations $|\zeta^n - \zeta^{n-1}|$ between successive iterates. Differences increase with subsequent iterations. Clearly the scheme does not converge in this case.

A slightly modified iterative approach (which was in fact first suggested by Accad and Pekeris (1978)) converges rapidly. The idea is to write

$$\zeta_{\text{SAL}} = \beta\zeta + (\mathcal{G}_{SAL} * \zeta - \beta\zeta) = \beta\zeta + \mathcal{G}'_{SAL} * \zeta, \tag{11}$$

where β is chosen to be a reasonable scalar SAL approximation (we used $\beta = 0.1$). At iteration $n+1$ we then replace $\zeta - \zeta_{\text{SAL}}$ in (1) with $(1-\beta)\zeta^{n+1} - \mathcal{G}'_{SAL} * \zeta^n$. It is readily verified that if this converges as $n \to \infty$, ζ^n converges to the solution of the full integro-differential equation. The change between successive iterates for this modified scheme, which converges in 4-5 iterations, are plotted as the solid line in Figure 2a. Note that the first iterate for this modified scheme (ζ^1) was forced with the full ζ_{SAL} computed from TPXO.5, and $\beta = 0$, so the first iteration is the same as for the simpler scheme.

In Figure 2b we plot the global integral of work done by the SAL term in the tidal equations

$$W_{SAL} = \left\langle \rho g \int\int \zeta_{\text{SAL}} \partial\zeta/\partial t) dS \right\rangle. \tag{12}$$

Since we assume an elastic Earth (with Love numbers strictly real) $\mathcal{G}_{SAL}$ is also real and the cycle average of the global integral must be zero (e.g., Egbert and Ray, 2001). W_{SAL} (computed with ζ obtained from iteration n and ζ_{SAL} from the previous) is plotted as a function of iteration number in Figure 2b. Note that for the initial iteration W_{SAL} is nearly 0.5 TW, a significant fraction of the 2.5 TW of M_2 tidal dissipation. For the modified (but not the simple) iterative scheme the W_{SAL} converges rapidly to zero, further demonstrating the consistency of ζ_{SAL} and ζ obtained in this way.

The iterative scheme for the SAL convolution suggests a possible refinement of our internal tide parameterization. Given a solution at iteration n, the currents $\mathbf{u}^n$ could be convolved with the Green's functions $\mathcal{G}_\omega$ to compute IT stress for each modeled tidal constituent. These in turn could be added as extra forcing terms for iteration $n+1$. A modification, comparable to that used for the SAL convolution, would be include the local linear drag tensor $\mathbf{R}$ in the model equations, and only add the deviation from this as a forcing. This proposed scheme would (if it converges!) allow for a frequency dependent, spatially non-local parameterization for IT drag. Since iteration for the SAL correction is already required, this may well require no additional runs of the SWE solver. However, we have not tested this scheme.

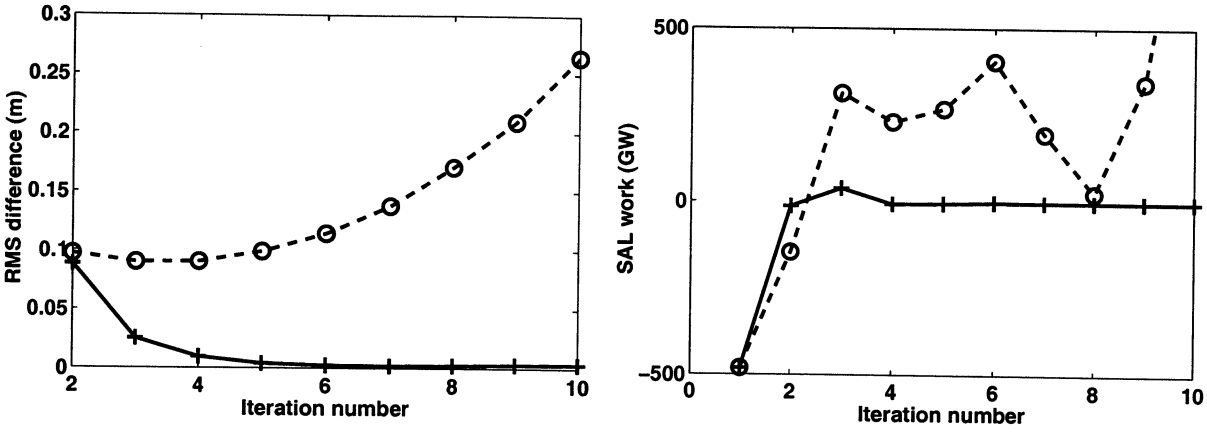

Figure 2: Convergence of iterative schemes for ocean self-attraction and tidal loading. (a) RMS difference in elevation between successive iterates, averaged over the globe. Dashed line: iterative scheme proposed by Hendershott (1972). Solid line: modified scheme of Accad and Pekeris (1978) described in text. (b) Convergence of global integral of SAL work term (12) for the simple (dashed lines) and modified (solid lines) iterative schemes. For all runs the IT drag parameterization based on (9) was used.

4 Results

4.1 Effect of Resolution

To assess how well the hydrodynamic solutions reproduce modern tidal elevations we compare model outputs with the global inverse solution TPXO.5. This reference model is most accurate in the open ocean, and equatorward of 66° where T/P data is available. The RMS difference between M_2 elevations computed using a wide range of grid resolutions and the T/P reference solution are plotted in Figure 3. Increasing resolution of the finite difference grid significantly improves agreement between model outputs and elevations inferred from T/P. This it true for model runs with and without an internal tide drag parameterization, and in deep and shallow water (Figure 3a). Including internal tide drag significantly reduces misfits for all resolutions. The best results, with misfits in deep water ($H > 1000$m) slightly below 5 cm RMS, are obtained with internal tide drag run at $1/12^\circ$ resolution. Only slightly worse results are obtained with a grid resolution of $1/8^\circ$. Including shallow seas in the comparison increases misfits somewhat (thiner lines in Figure 3a). The work done by the tidal potential, which must equal the global tidal energy dissipation, also converges to approximately the proper value (of approximately 2.5 TW) as resolution is increased. The agreement is better (especially at lower resolution) when the IT drag parameterization is used.

For the results presented in Figure 3 internal tide drag was parameterized in terms of

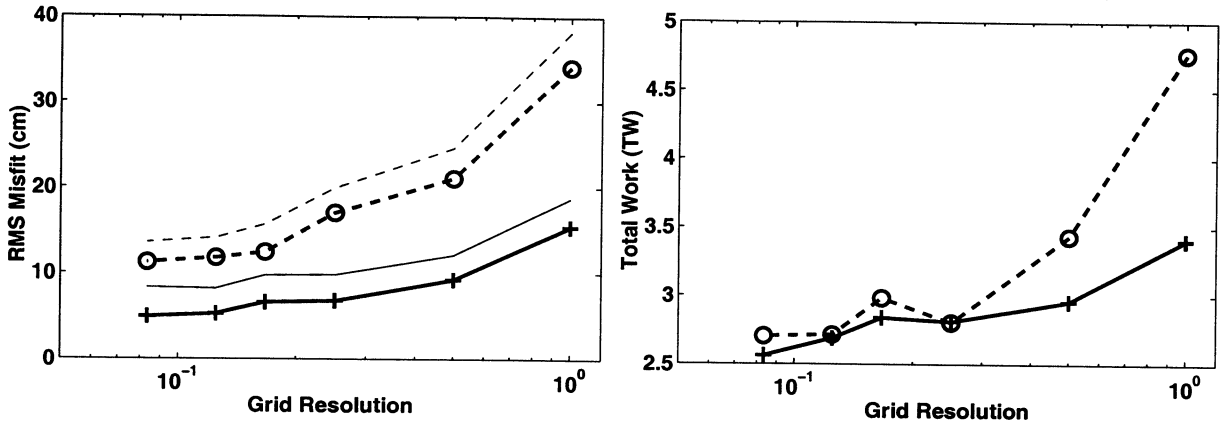

Figure 3: (a) RMS difference between M_2 elevations from the T/P global inverse solutions TPXO.5, and hydrodynamic solutions computed at a range of grid resolutions. Solid and dashed lines are for computations with and without internal tide drag respectively. Heavy lines marked with circles and pluses give misfits for deep ($H > 1000$m) water; the light lines give misfits for the full globe (equatorward of 66°). (b) Global integral of work done by the M_2 tidal potential, for solutions with (solid lines) and without (dashed lines) internal tide drag, for solutions at a range of resolutions.

the linear drag tensor $\mathbf{R}$ defined in (9), without adjusting any parameters. Very similar results were obtained with the other two IT drag parameterizations discussed above, but in these cases some tuning of the overall scale of the IT drag was required. For the scheme based on Bell's (1972) formula (4) we found results were best for a value of $\kappa \approx 10^{-3}\mathrm{m}^{-1}$, slightly larger than the optimal value $\kappa \approx 2\pi \times 10^{-4}\mathrm{m}^{-1}$ found by Jayne and St. Laurent (2001). For the third scheme IT drag coefficients derived from Sjoberg and Stigebrandt (1992) (computed using bathymetry on a $1/12^\circ$ grid), worked best when multiplied by a factor of 0.75.

4.2 Sensitivity to Errors in Bathymetry

Figure 3 suggests that further increases in grid resolution will lead to little improvement in fit to the observed modern tidal elevations. A number of factors probably limit the accuracy that can be expected from numerical solution of the SWE at any resolution. For example, the IT drag parameterizations we have tested are all based on a linear treatment of small amplitude topography. Even for this simplified linear case a proper treatment of IT drag would involve convolution with a non-local operator, so we have only incorporated IT drag approximately. The parameterization of bottom drag in terms of (3) with a constant c_D, or of subgrid scale motions in terms of an eddy diffusivity, must also be only approximately correct. And of course, even for the modern ocean, there are potentially significant errors in the available bathymetric databases.

Case	Global RMS (cm)	Deep Ocean RMS (cm)
5% errors	3.23	2.69
10% errors	8.17	6.65
Variable errors	8.23	6.67

Table 1: Root mean square changes in M_2 tidal elevations due to random variations of bathymetry.

To test the sensitivity of model solutions to bathymetric errors we did a series of runs with small random perturbations to our standard bathymetry. To save on computer time these runs were all done on a $1/4^\circ$ grid. Several scenarios for the bathymetry errors were considered. In each case 10 perturbed bathymetric grids were generated, solutions were calculated for each, and the global RMS elevation differences (relative to the standard bathymetry solution) were computed. Results are summarized in Table 1. For the first case the random variations were 5% of the local depth, with a decorrelation length scale of 2.5°. For the second case error amplitudes were increased to 10%, and for the third variable error magnitudes were assumed, with a dependence on depth modeled on the statistics of differences between the Gtopo30 (Smith and Sandwell, 1997) and ETOPO5 (National Geophysical Data Center, 1992) databases, which were found to be: $H < 100$m: 25%; 100 m$< H <$ 200 m: 15%; 200 m$< H <$ 1000 m: 10%; 1000 m$< H <$ 3000 m: 6%; $H >$ 3000 m: 3%. For cases 2 and 3 the decorrelation length scale of the bathymetric errors remained 2.5°.

As another test of sensitivity of model elevations to bathymetric inputs, we ran the model with bathymetry derived directly from the ETOPO5 database alone. RMS differences of M_2 elevations between this solution and that from our standard bathymetry case (again computed on a $1/4^\circ$ grid) were 11.8 cm (all depths), and 6.9 cm ($H >$ 1000m). This last result is at least roughly consistent with the sensitivity inferred from our experiments with random depth errors. It is difficult to assess the accuracy of the Gtopo30 bathymetry. However, even if errors are only half the size of the difference between Gtopo30 and ETOPO5 (perhaps an optimistic assessment), Table 1 suggests that open ocean errors in modeled M_2 tidal elevations of 3–4 cm RMS should be expected. Given the other shortcomings in the numerical SWE model, the 5 cm RMS error achieved by our $1/12^\circ$ model is probably already approaching the lower limit of M_2 tidal modeling errors that can be achieved at present. The high sensitivity of model outputs to bathymetry also implies that it will be very difficult to model ocean tides accurately in the distant past.

4.3 M_2 Tides in the Last Glacial Maximum (LGM)

With the hydrodynamic model tuned to model the present ocean tides, we consider the effect of dropping sea–level to that inferred for the LGM. For these experiments Bathy-

metric grids were modified using the 1° topography and ice model ICE-4G (Peltier, 1993; 1994). For each time considered (5, 10, 15, 20 ka), we computed the difference in ocean depth with the present day (0 ka) ICE-4G topography. The difference fields were then interpolated onto our $1/8^{\circ}$ nearly global grid, and added to the present day bathymetry. In this manner we made sea–level adjustments consistent with the resolution of ICE-4G, but retained the higher resolution bathymetric details of the modern topography. We did these numerical experiments at $1/8^{\circ}$ (instead of $1/12^{\circ}$) to economize on computer time. In Figure 4a we plot RMS difference between the present day tidal elevations (as determined by T/P), and the elevations computed from a series of times over the past 20 kyr. This figure reveals that M_2 tidal elevations in the LGM were indeed significantly different.

In Figure 4b we plot M_2 tidal dissipation (inferred from the astronomical work) in the numerical solutions for the past 20 kyr. A significant increase in dissipation, by approximately 40% or more, accompanies the drop in sea-level which exposed many of the shallow shelf areas where present day dissipation is greatest.

For the results of Figure 4 we have kept the IT drag tensor exactly as estimated for the modern ocean. Since this depends strongly on stratification this extra frictional term may not be appropriate for the LGM. (The IT drag based on (9) also depends, but much more weakly, on the tidal currents. Note that with the other two formulations tried the estimated coefficients depend *only* on the bathymetric gradient and the stratification.) As a sensitivity test we did computations for 20 ka with IT drag coefficients reduced and increased (uniformly across the globe) from our estimates based on the modern stratification. The first case, which corresponds to a significant decrease in stratification, results in further increases in tidal dissipation to over 4 TW. For the second case (with increased IT friction) total dissipation is reduced, and elevations are somewhat more consistent with those of the present day.

In Figure 5 we plot M_2 elevation amplitude and phase for the modern day and 20 ka $1/8^{\circ}$ M_2 tidal solutions, computed with the standard IT drag parameterization, and the 20 ka solution computed with IT drag coefficients reduced by a factor of 4. Note that the color scale for the amplitudes is logarithmic. Amplitudes for the 20 ka solutions are noticeably larger throughout the ocean. Amplitude increases are especially great in the North Atlantic, where tidal amplitudes in the 20 ka model solution exceed 3–4 m over much of the Labrador Sea, and off the Atlantic coasts of Spain and North Africa. Reducing the IT drag coefficient results in further increases in amplitude. For this case more significant amplitude increases also occur in the Pacific basin, especially off the east coast of Australia and around New Zealand.

In Figure 6 the distribution of tidal energy dissipation is plotted for the three numerical solutions of Figure 5, and for the solution computed with present day topography but no internal tide drag. For these calculations we followed the approach described in Egbert

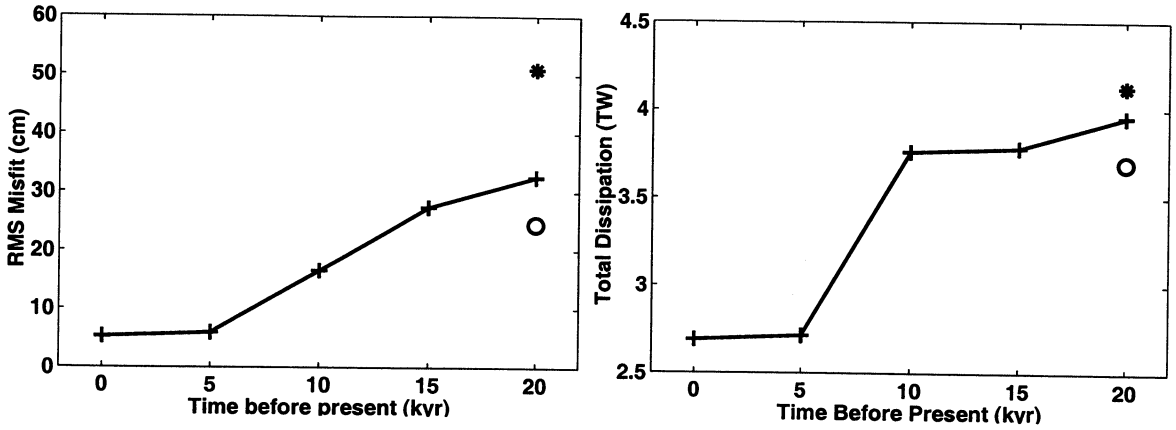

Figure 4: (a) RMS misfit to modern tidal elevations for solutions computed with bathymetry appropriate to the past 20 kyr. (b) Work done by the tidal potential over this time. The asterisks and open circles at 20 ka are for the cases with IT drag multiplied by 0.25 and 2, respectively.

	TPXO.5	GOT99hf	0 ka IT	0 ka no IT	20 ka IT	20 ka IT×.25	20 ka IT×2
Shallow	1.625	1.717	2.104	2.644	2.443	3.088	1.877
Deep	.813	.729	.576	.061	1.513	1.038	1.817
Total	2.438	2.446	2.680	2.705	3.956	4.126	3.694

Table 2: Dissipation (in TW) in deep and shallow seas, following the division given in Egbert and Ray (2001). TPXO.5 and GOT99hf are constrained by T/P data, the other 4 are purely numerical solutions discussed in text.

and Ray (2001), with dissipation computed as a local balance between energy flux divergence and work done by the tide generating force and SAL. A rough breakdown between dissipation in shallow seas and the deep ocean, is given in Table 1 for these four solutions, and for the 20 ka solution with IT drag increased by a factor of 2. For comparison, results from two of the T/P constrained solutions from Egbert and Ray are also given here. A more detailed breakdown for the shallow seas and deep-ocean areas discussed in Egbert and Ray (2001) is given in Figure 7 for all 5 of the numerical solutions and TPXO.5.

Figure 7 reveals fairly good agreement between the spatial distribution of dissipation in the 0 ka solution (with IT drag) and in the T/P constrained solution TPXO.5. The most significant discrepancies in shallow seas are in the Arctic, along the West coast of North America and around New Zealand. In all of these areas the numerical model dissipates more energy than the T/P based estimates suggest. Note that areas around Indonesia are poorly constrained by the T/P data, as discussed in Egbert and Ray (2001). In deep water, areas in the South Pacific (Micronesia/Melanesia and Polynesia) come out high in the numerical solution, while the Mid-Atlantic and W. Indian Ridges come out low. This suggests that our IT parameterization overestimates drag produced over the larger scale

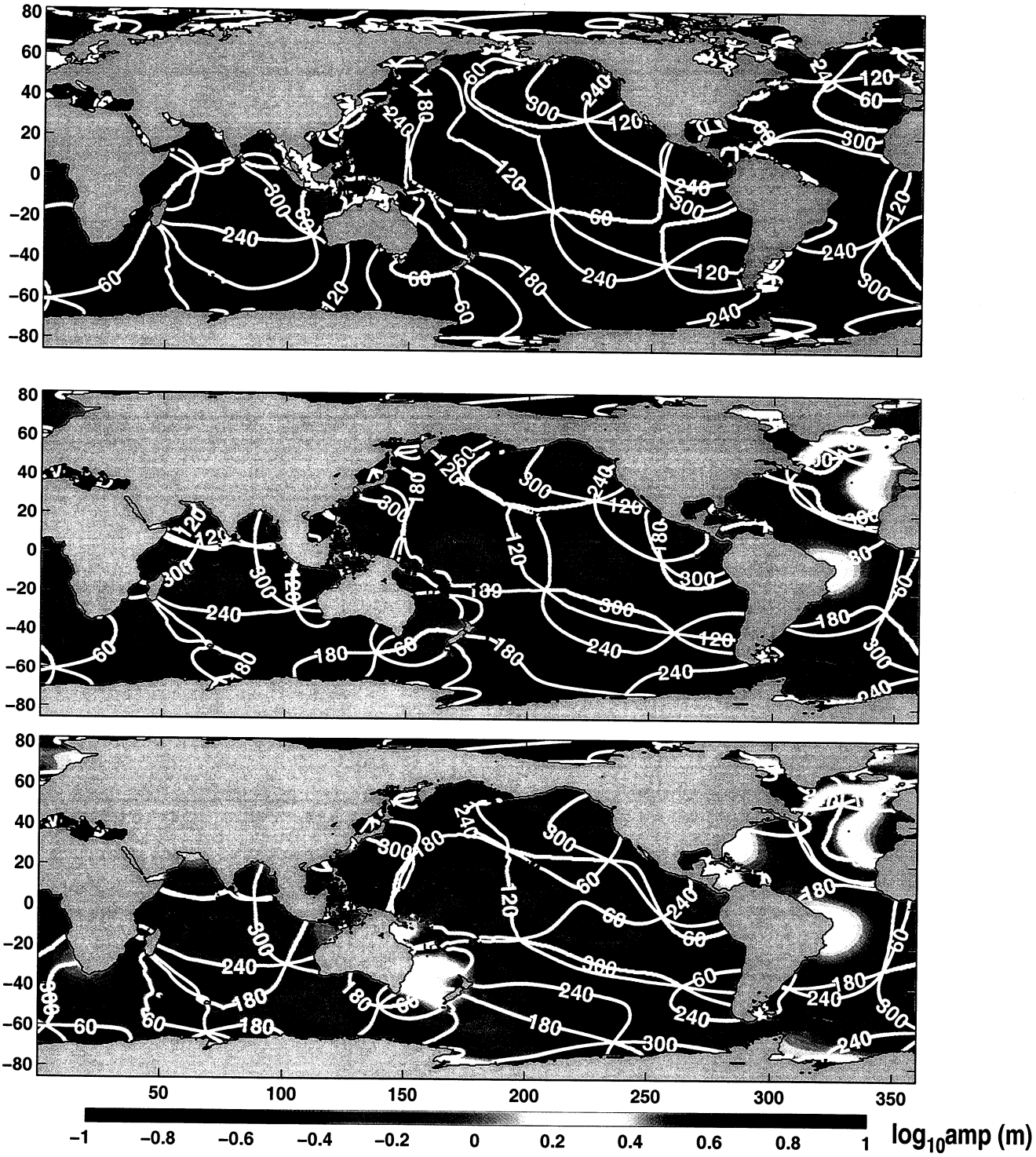

Figure 5: Amplitude and phase of M_2 tidal solutions for the present (top) and 20 ka (middle), computed with the standard IT drag, and for 20 ka computed with IT drag coefficients multiplied by 0.25 (bottom). Note that a logarithmic scale is used for amplitudes.

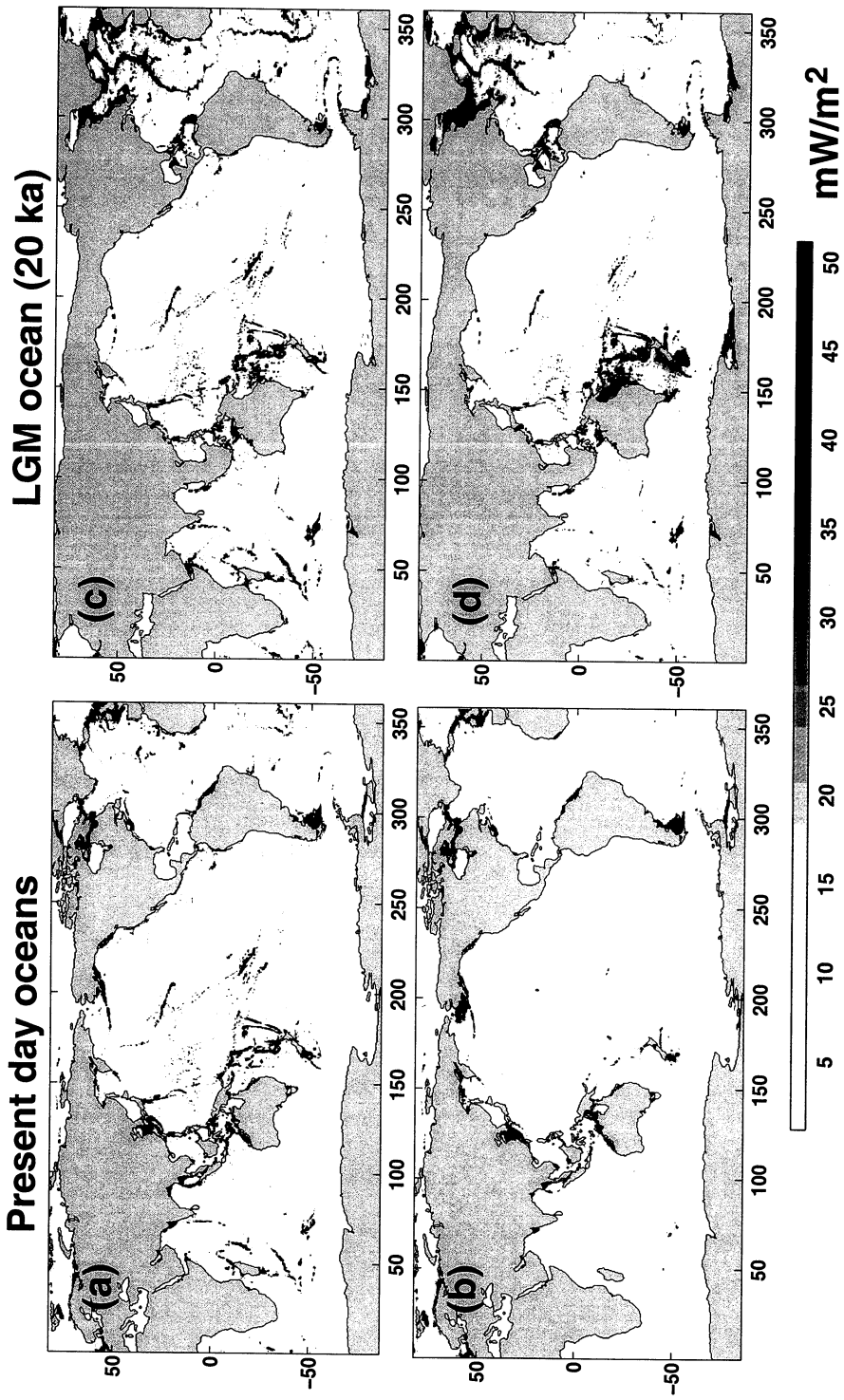

Figure 6: Spatial distribution of dissipation computed for the numerical solutions as the balance between energy flux divergence and work terms. Solution were computed using present day bathymetry with (a) and without (b) IT drag parameterization; and for 20 ka bathymetry with IT drag from the present day (c) and reduced by a factor of 4 (d).

topography associated with volcanic arcs and island chains, and underestimates drag over oceanic spreading centers, which are dominated by smaller spatial scales, and are spread over a larger area. Turning off the IT drag of course nearly eliminates dissipation in all of the deep ocean areas. It also causes significant increases in dissipation in a number of shallow seas, especially in area (1), which includes the Labrador sea and all points north and west into Hudson Bay, on the Patagonian and European Shelves, and in the Bering Sea.

As Figures 6 and 7 and Table 2 show, dramatic changes to the distribution of tidal energy dissipation are likely to result from the drop in sea-level of the LGM. Some of the major shallow sea sinks from the present day ocean are significantly reduced in area, and as a result would dissipate little energy. These include the Yellow Sea, the shelf off the northeast coast of Brazil, and the Andaman Sea. Dissipation is also significantly reduced over the European and Patagonian shelves and in the Gulf of Maine off the east coast of North America. Dissipation in some other areas increases dramatically in the model solutions for 20 ka. These include the Hudson Bay/Labrador Sea area, the Arctic (including here the Norwegian sea) and Antarctic, and the area around the Caribbean. The dissipation in this last area is concentrated over the volcanic arc on the eastern edge of this area, and almost all of the dissipation is in fact associated with IT drag, rather than bottom boundary layer processes in shallow seas. This is just one of the areas around the North Atlantic where tidal dissipation increases dramatically in the LGM. There are also significant increases for the Mid-Atlantic Ridge (especially in the North Atlantic; see Figure 6), and off the northwest coast of Africa.

When IT drag is also reduced by a factor of 4 for the 20 ka bathymetry, further significant increases are observed in the Hudson Bay region, the Arctic and Antarctic, and on the Eastern edge of the Caribbean. Each of these areas now accounts for a rather astounding (by the standards of the present day ocean) 400-600 GW. Dissipation is reduced in some, but not all, deep ocean areas. Thus significant reductions in the drag coefficients are counterbalanced to some extent by increases in tidal current velocities. Thus while the IT drag coefficient is reduced by a factor of 4, dissipation in the deep ocean areas (where IT drag is by far dominant) is only reduced by a factor of 1.5 overall (Table 2). Figure 6d provides a striking image of the redistribution in tidal dissipation that would result from this (rather hypothetical) change in IT drag coupled with the drop in sea-level. In this case there are three centers of tidal dissipation, in the North Atlantic, in the seas around New Zealand, and around Antarctica.

Increasing IT drag by a factor of 2 for the 20 ka bathymetry results in less obvious changes in the distribution of dissipation. However dissipation in the deep water is increased somewhat (Table 2), especially along the Mid-Atlantic and West Indian Ridges.

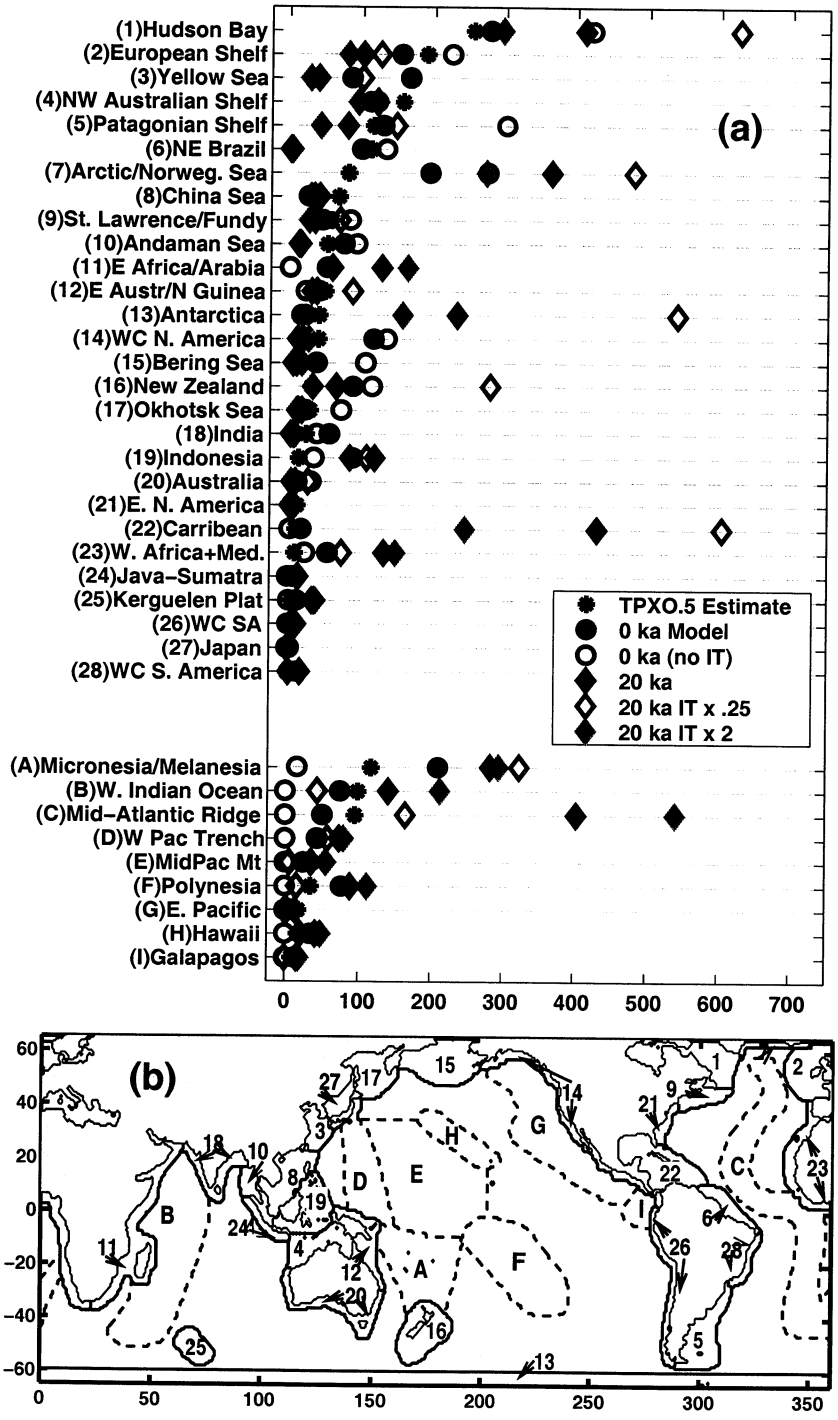

Figure 7: (a)Energy dissipation integrated over shallow seas and selected deep ocean areas defined in (b).

5 Conclusions

Efforts to develop a purely hydrodynamic model of the present day tides have been reasonably successful. A convergent iterative scheme for rigorous treatment of SAL has been developed, and three different approaches to parameterization of IT drag have been tried. Both the rigorous treatment of SAL and IT drag parameterizations are required to obtain agreement with the highly accurate T/P constrained tidal solutions for the present day ocean. Success with the numerical modeling also required high resolution numerical grids and accurate bathymetry. Limitations in our ability to reproduce the present day tides are probably due to errors in bathymetry, and probably also our approximate linear theory for computing IT drag.

After achieving reasonable accuracy for the present day tides, the hydrodynamic model was run with bathymetry estimated for a series of times over the past 20 ka, extending into the LGM. The drop in sea-level associated with the LGM is found to result in significant changes in tidal fields, and increases of 40-50% in total dissipation. However, details are sensitive to stratification, and this is much more poorly known than bathymetry in the recent past. The full implications of the predicted changes in LGM tides remain to be explored.

References

[1] Accad, Y., and C. L. Pekeris, Solution of the tidal equations for the $Msub2$ and $Ssub2$ tides in the world oceans from a knowledge of the tidal potential alone, *Phil. Trans. R. Soc. London, 290*, 235–266, 1978.

[2] Baines, P. G., On internal tide generation models, *Deep Sea Res., 29,* 307–338, 1982.

[3] Bell, T.H., Topographically generated internal waves in the open ocean, *J. Geophys. Res., 80*, 320–327, 1975.

[4] Bills, B.G., and R. D. Ray, Evolution of the lunar orbit: a synthesis of recent results, *Geophys. Res. Lett., 26*, 3045–3048, 1999.

[5] Egbert, G.D., Tidal data inversion: Interpolation and Inference, *Prog. Ocean., 40,* 53-80, 1998.

[6] Egbert, G. D., A. F. Bennett, M. G. G. Foreman, Topex/Poseidon tides estimated using a global inverse model, *Jour. Geophys. Res., 99,* 24821–24852, 1994.

[7] Egbert, G. D., and R. D. Ray, Significant tidal dissipation in the deep ocean inferred from satelite altimeter data, *Nature, 405*, 775–778, 2000.

[8] Egbert, G.D. and R.D. Ray, Estimates of M2 Tidal Energy Dissipation from TOPEX POSEIDON Altimeter Data, *J. Geophys. Res., 106*, 22,475–22,502, 2001.

[9] Garrett, C., S. Stringer, and L. St. Laurent, Simple models of internal tide generation at abrupt topography, Ocean Science Meeting, Amer. Geophys. Union, Honlulu, HI, 11-15 Feb., 2002.

[10] Gustafsson, K.E., Comparison of the energy flux to mixing processes via baroclinic wave drag on barotropic tides, *Deep Sea Res., 48*, 2283–2296, 2001.

[11] Hendershott, M., The effects of solid earth deformation on global ocean tides, *Geophys. J. R. Astron. Soc., 29*, 389–403, 1972.

[12] Hendershott, M. C., Numerical models of ocean tides, in *The Sea*, vol. 6, *Marine Modelling,* edited by E. Goldberg et al., pp. 47–95, John Wiley, New York, 1977.

[13] Jayne, S. R., and L. C. St. Laurent, Parameterizing tidal dissipation over rough topography, *Geophys. Res. Lett., 28*, 811–814, 2001.

[14] Le Provost, C. L., M. L. Genco, F. Lyard, P. Vancent, and P. Canceil, Spectroscopy of the world ocean tides from a hydrodynamic finite element model, *J. Geophys. Res., 99,* 24,777–24,797, 1994.

[15] Llewellyn Smith, S. G., and W. R. Young, Conversion of the barotropic tide, submitted to *J. Phys. Ocean.*, 2001.

[16] Levitus, S., Levitus 1982 annual climatology from DODS datasets Goddard DAAC, NASA, Greenbelt, Md., 1999.

[17] Lyard, F., and M. L. Genco, Optimization methods for bathymetry and open boundary conditions in a finite element model of ocean tides, *J. Comput. Phys., 114*, 234–256, 1994.

[18] Peltier, W., Time Dependent Topography Through Glacial Cycle, IGBP PAGES/World Data Center-A for Paleoclimatology Data Contribution Series # 93-015, NOAA/NGDC, Paleoclimatology Program, Boulder CO, USA, 1993.

[19] Peltier, W. R., Ice Age Paleotopography, *Science, 265,* 195-201, 1994.

[20] Ray, R. D., Ocean self-attraction and loading in numerical tidal models, *Marine Geodesy, 21,* 181-192, 1998.

[21] Schrama, E. J. O., and R. D. Ray, A preliminary tidal analysis of TOPEX/Poseidon altimetry, *Jour. Geophys. Res., 99*, 24,799–24,808, 1994.

[22] Shum, C. K., et al., Accuracy assessment of recent ocean tide models, *Jour. Geophys. Res., 102*, 25,173–25,194, 1997.

[23] Schwiderski, E. W., Global ocean tides, Part I: a detailed hydrodynamical interpolation model, NSWC/DL TR-3866, Naval Surface Weapons Center, Dahlgren, VA., 1978.

[24] Sjoberg, B. and A. Stigebrandt, Computations of the geographical distribution of the energy flux to mixing processes via internal tides and the associated vertical circulation in the ocean, *Deep Sea Res., 39,* 269–291, 1992.

[25] Smith, W. H. F., and D. T. Sandwell, Global sea floor topography from satellite altimetry and ship depth soundings, *Science, 277,* 1956–1962, 1997.

[26] Thomas, M., and J. Sundermann, Tides and tidal torques of the world ocean since the last glacial maximum, *J. Geophys. Res., 104,* 3159–3183, 1999.

REPORT DOCUMENTATION PAGE

Form Approved
OMB No. 0704-0188

1. AGENCY USE ONLY (Leave blank)	2. REPORT DATE	3. REPORT TYPE AND DATES COVERED
	3-05-02	Final 9/15/97 - 9/14/01

4. TITLE AND SUBTITLE
Orbital, Rotational and Climatic Interactions: Energy Dissipation and Angular Momentum Exchange in the Earth-Moon System

5. FUNDING NUMBERS
NAG5-6156

6. AUTHOR(S)
Gary D. Egbert

7. PERFORMING ORGANIZATION NAME(S) AND ADDRESS(ES)
OSU
Corvallis, OR 9733

8. PERFORMING ORGANIZATION REPORT NUMBER
NS068A

9. SPONSORING/MONITORING AGENCY NAME(S) AND ADDRESS(ES)
ONR

10. SPONSORING/MONITORING AGENCY REPORT NUMBER

11. SUPPLEMENTARY NOTES

12a. DISTRIBUTION/AVAILABILITY STATEMENT
Unlimited Public Access

12b. DISTRIBUTION CODE

13. ABSTRACT

Summary. A numerical ocean tide model has been developed and tested using highly accurate TOPEX/Poseidon (T/P) tidal solutions. The hydrodynamic model is based on time stepping a finite difference approximation to the non-linear shallow water equations. Two novel features of our implementation are a rigorous treatment of self attraction and loading (SAL), and a physically based parameterization for internal tide (IT) radiation drag. The model was run for a range of grid resolutions, and with variations in model parameters and bathymetry. For a rational treatment of SAL and IT drag, the model run at high resolution (1/12 degree) fits the T/P solutions to within 5 cm RMS in the open ocean. Both the rigorous SAL treatment and the IT drag parameterization are required to obtain solutions of this quality. The sensitivity of the solution to perturbations in bathymetry suggest that the fit to T/P is probably now limited by errors in this critical input. Since the model is not constrained by any data, we can test the effect of dropping sea-level to match estimated bathymetry from the last glacial maximum (LGM). Our results suggest that the $\approx$ 100 m drop in sea-level in the LGM would have significantly increased tidal amplitudes in the North Atlantic, and increased overall tidal dissipation by about 40%. However, details in tidal solutions for the past 20 ka are sensitive to the assumed stratification. IT drag accounts for a significant fraction of dissipation, especially in the LGM when large areas of present day shallow sea were exposed, and this parameter is poorly constrained at present

14. SUBJECT TERMS

15. NUMBER OF PAGES

16. PRICE CODE

17. SECURITY CLASSIFICATION OF REPORT	18. SECURITY CLASSIFICATION OF THIS PAGE	19. SECURITY CLASSIFICATION OF ABSTRACT	20. LIMITATION OF ABSTRACT